Identification of trapping finer-scale fluctuations in a solitary vortex in linear magnetized plasma

Hiroyuki Arakawa, Makoto Sasaki, Shigeru Inagaki, Maxime Lesur, Yusuke Kosuga, Tatsuya Kobayashi, Fumiyoshi Kin, Takuma Yamada, Yoshihiko Nagashima, Akihide Fujisawa, et al.

Identification of trapping finer-scale fluctuations in a solitary vortex in linear magnetized plasma

H. Arakawa
Department of Health Sciences, Faculty of Medical Sciences, Kyushu University, Fukuoka 812-8582, Japan
E-mail: arakawa.hiroyuki.306@m.kyushu-u.ac.jp

M. Sasaki
College of Industrial Technology, Nihon University, Narashino 275-8575, Japan

S. Inagaki
Institute of Advanced Energy, Kyoto University, Uji 611-0011, Japan
Research Center for Plasma Turbulence, Kyushu University, Kasuga 816-8580, Japan

M. Lesur
Université de Lorraine, CNRS, IJL, Nancy F-54000, France

Y. Kosuga
Research Institute for Applied Mechanics, Kyushu University, Kasuga 816-8580, Japan
Research Center for Plasma Turbulence, Kyushu University, Kasuga 816-8580, Japan

T. Kobayashi
National Institute for Fusion Science, National Institutes of Natural Sciences, Toki 502-5292, Japan
Research Institute for Applied Mechanics, Kyushu University, Kasuga 816-8580, Japan

F. Kin
Institute of Advanced Energy, Kyoto University, Uji 611-0011, Japan

T. Yamada
Faculty of Arts and Science, Kyushu University, Fukuoka 819-0395, Japan
Research Center for Plasma Turbulence, Kyushu University, Kasuga 816-8580, Japan

Y. Nagashima
Research Institute for Applied Mechanics, Kyushu University, Kasuga 816-8580, Japan

Research Center for Plasma Turbulence, Kyushu University, Kasuga 816-8580, Japan

A. Fujisawa

Research Institute for Applied Mechanics, Kyushu University, Kasuga 816-8580, Japan
Research Center for Plasma Turbulence, Kyushu University, Kasuga 816-8580, Japan

K. Itoh

Frontier Research Institute, Chubu University, Kasugai 487-8501, Japan
Research Center for Plasma Turbulence, Kyushu University, Kasuga 816-8580, Japan
National Institute for Fusion Science, National Institutes of Natural Sciences, Toki 502-5292, Japan

16 August 2023

Abstract. The mutual interaction of drift wave-type modes and zonal flows causes the formation of higher-order nonlinear structures. This study focuses on the spatio-temporal behaviour of these higher-order structures in a linear magnetized plasma. The structures include a solitary vortex, a long-lived circumnavigating motion localized both radially and azimuthally, and a short-lived packet of finer-scale fluctuations excited at the position of the solitary vortex. Observing the time evolution of the two-dimensional cross-sectional structures revealed that the packet of finer-scale fluctuations is trapped in the solitary vortex. The trapping times found are consistent with the theoretical evaluation.

Keywords: magnetized plasma, Zonal flow, solitary vortex, finer-scale fluctuations, higher-order nonlinear structure, two-dimensional cross-sectional structure

Submitted to: *Plasma Phys. Control. Fusion*

1. Introduction

Dynamic interactions between linearly unstable drift wave and secondarily nonlinearly generated zonal flows [1, 2] have been actively investigated in plasma turbulence owing to its significant influence on plasma transport [3, 4, 5]. Geodesic acoustic modes (GAMs), an oscillating branch of zonal flows specific to toroidal plasmas, have also been the subject of many studies [6]. The physics related to the interaction between drift-wave and zonal flows is considered to share a common, somewhat universal nature, at least from linear magnetized plasmas to toroidal fusion plasmas. Consequently, research has been advanced in fundamental linear magnetized plasmas. For instance, investigations into the intrinsic nature of drift waves [7], transitions from drift wave to turbulence [8],

direct observations of zonal flow generation [9], and interactions between drift wave and zonal flows [10, 11, 12, 13] have been conducted.

Theoretical and simulation studies suggest that spatio-temporal dynamics of drift waves interacting with zonal flows can be significantly influenced by the trapping of higher-order, nonlinearly excited coherent structures. The trapping in zonal flows has been found by P. Kaw *et.al.* [14], as a result of phase-space dynamics (formation of coherent vortex in the phase-space). The trapping mechanism has also been applied to the interaction between drift wave and GAMs [15, 16, 17]. In this context, the spatial localization of the structures by the stationary zonal flows [18], and the azimuthal bunching of the structures by the streamer [19] have been found to be caused by the trapping. The trapping mechanism is independent of magnetic field configurations, so that it should be possible to validate the mechanism in linear magnetized plasmas. However, the trapping of the structures has not yet been directly observed experimentally and as such should be demonstrated.

Our recent experimental studies of linear magnetized plasma observed higher-order coherent structures in the system of drift wave-type modes and the secondary nonlinearly generated zonal flow [20]. The higher-order structures includes a spatially localized, long-lived solitary vortex and short-lived packet of finer-scale fluctuations. The solitary vortex is excited by the interaction between the drift wave-type modes and the zonal flow [21]. The finer-scale fluctuations (termed "splash" in [20]) have shorter lifetimes and excited at the same azimutual position as the solitary vortex [20]. However, the finer-scale fluctuations were only observed at a specific radial position, and temporal variations in the two-dimensional cross-sections had not been obtained.

In this study, we experimentally identified the trapping of the finer-scale fluctuations in a solitary vortex in linear magnetized plasma. The time-resolved two-dimensional analysis allows us to observe linearly unstable drift wave-type modes and the secondary nonlinearly generated zonal flow, as well as the solitary vortex and the short-lived packet of finer-scale fluctuations. The trajectory of the finer-scale fluctuations circulating in the solitary vortex is detected, demonstrating that they are trapped in the solitary vortex. The time at which finer-scale fluctuations were trapped was in close agreement with the theoretical evaluation.

2. Experimental setup

A cylindrical argon plasma with a diameter of $\sim$0.1 m and an axial length of 3.74 m was produced at a linear plasma device, LMD-U [20]. The plasma was excited by radio frequency (RF) waves and was radially bounded by a magnetic field with no external source of momentum. The operational parameters are 3 kW RF power, 900 G magnetic field strength (B), and 0.68 Pa argon gas pressure. Typical plasma parameters are central plasma density of $\sim 6 \times 10^{18}$ m^{-3} and $\sim$2.5 eV electron temperature ($T_{\rm e}$). The major diagnostic tools used in this study are two multi-channel arrays of Langmuir probes. One is an azimuthal array with 64 probes located at a radius of $r = 4$ cm,

which is the position where the density gradient is at its maximum. Another array consists of three radially movable probes with a range of $r = 1.5$–7 cm. The Langmuir probes measure the ion saturation current ($I_{\rm is}$) and the floating potential ($V_{\rm f}$), which are roughly proportional to the electron density and the plasma potential, respectively. These measures are obtained simultaneously during each discharge (0.5 s) and sampled at a frequency of 1 MHz.

3. Fundamental observations

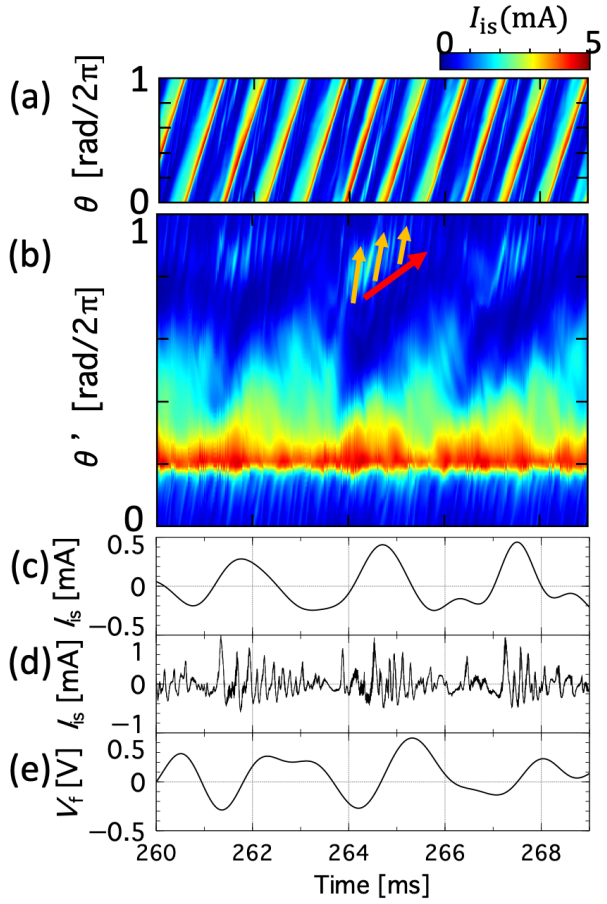

Figure 1. (a) Spatio-temporal behaviour of the ion saturation current ($I_{\rm is}$) at a radius of $r = 4$ cm. The positive direction of the vertical axis corresponds to the electron diamagnetic direction. (b) Galilean transformed (a). The azimuthal angle (θ) of the vertical axis in (a) is transformed to $\theta' = \theta$ - $v_p t$, where v_p denotes the phase velocity of the nonlinear wave. The red arrow indicates the propagation of a solitary vortex and the yellow arrows highlight the propagation of the packet of finer-scale fluctuations. (c) Temporal behaviour of $I_{\rm is}$ for the solitary vortex (d) and for the packets of finer-scale fluctuations. (e) Temporal behaviour of $V_{\rm f}$ of the zonal flow.

Figure 1(a) shows the dependence in time and azimuthal angle of $I_{\rm is}$ at $r = 4$ cm by the azimuthal probe array. The steep density peeks steadily propagates in the electron

diamagnetic direction. The fundamental mode ($m = 1$, $f_{DW} = 1.2$ kHz) and its higher harmonics have the same phase velocity, where m is the azimuthal mode number, which is related to the wavenumber (k_θ) via the expression, $m = rk_\theta$. As the fundamental mode is observed in a region with a steep density gradient ($\nabla n/n \sim 100$ m^{-1}). The linear dispersion relation of the drift wave is given by $f_{DW} = (k_\theta \frac{T_e}{eB} \frac{\nabla n}{n})/(1 + \rho^2 k_\theta^2) \cdot \frac{1}{2\pi} \sim 1.8$ kHz, which aligns closely with our experimental observation of f_{DW}. Consequently, the mode is considered to be of the drift wave-type. Here, the drift wave-type mode and its harmonics is referred to as the waves.

To understand how the solitary vortex and the packet of finer-scale fluctuations are excited, a Galilean transform is applied to Fig. 1(a); the linear phase shift in the azimuthal angle along the propagation direction of the waves are subtracted. The results are shown in Fig. 1(b). The red and yellow arrows in the figure display the density peaks of the solitary vortex and packet of finer-scale fluctuations. The solitary vortex and the packet of finer-scale fluctuations propagate at 2.6×10^3 π rad/s and $4 \times 10^3 \pi$ rad/s, respectively, in the laboratory frame. A frequency filter (<1 kHz or >1 kHz) was applied to Fig. 1(b) at the transformed azimuthal angle $\theta' = 0.9\,\mathrm{rad}/2\pi$ and was demonstrated in Figs. 1(c) and (d). The excitation/damping of the density in the solitary vortex and the amplitude envelope of the finer-scale fluctuations are synchronized at a frequency of ~ 0.4 kHz. The temporal evolution of the floating potential fluctuation (0.1–1 kHz) at $r = 4$ cm by the radially movable is shown in Fig. 1 (e). The figure indicates that the potential is also synchronized with the frequency of the solitary vortex and the amplitude envelope of the finer-scale fluctuations. Our previous studies reveal the existence of the zonal flow in these experimental conditions [22, 20]. The zonal flow has a frequency of about 0.4 kHz and a radial wavenumber of 0.8π rad cm^{-1}. Compared to the typical period of the waves, the solitary vortex has a long lifetime ($\sim$1.2 ms, which is equal to half of the typical zonal flow period), while the packet of finer-scale fluctuations has a short lifetime (around 0.2 ms at this radius).

As the zonal flow and the waves interact, the waveform of the waves is modified by the frequency of the zonal flow as it propagates [21]. This change stems from the modulation of the fundamental mode, which subsequently affects the amplitude and phase relationship with the harmonic waves. This leads to the formation of a solitary vortex [21]. The excitation of finer-scale fluctuations is also synchronized with this process.

4. Reconstruction of two-dimensional structure

To understand the propagation in the radial-azimuthal cross-section of the finer-scale fluctuations, a modified template method was used with the data collected from the azimuthal probe array and the radially movable probe array. The template method [23] is a technique of conditional averaging of structures based on the correlation coefficient between a reference waveform and the time-varying waveform. The modified template method is a two-dimensional extension of the one-dimensional template method for

structure extraction in turbulence.

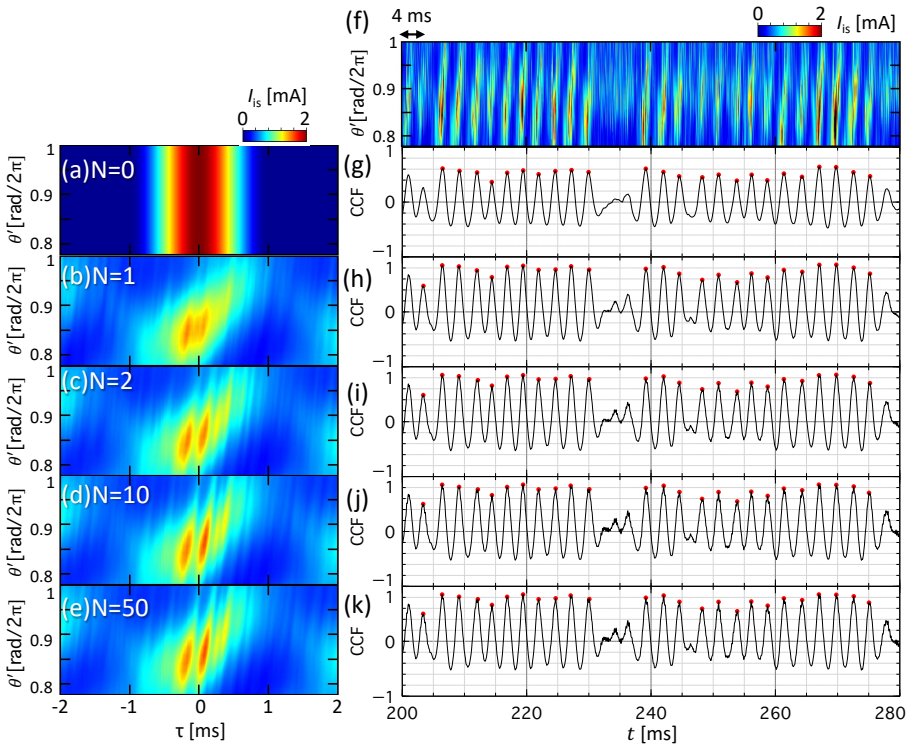

Figure 2. The process of two-dimensional reference waveform generated by the template method. (a)–(e) Iterative reference waveform with $N = 0$, 1, 2, 10 and 50, where N denotes the iteration number. The resulting reference waveform is (e). (f) Spatio-temporal $I_{\rm is}$ of a partial azimuthal range, $\theta' = 0.78 - 1.0$ rad/2π, where the Galilean transform was applied. (g)–(k) Cross-correlation function (CCF) between the N-th reference waveform and spatio-temporal $I_{\rm is}$ ((f)). The red points indicate the correlation peaks.

Here, the reference waveform was generated in the following iterative manner [23]. Initially, the reference waveform was a cosine function that was uniform in the azimuthal angle, as illustrated in Fig. 2(a). The cross-correlation function between this initial reference waveform (denoted as $N = 0$, Fig.2(a)) and the spatio-temporal $I_{\rm is}$ from the azimuthal probe array (Fig.2(f)) was calculated. For this analysis, we selected a specific azimuthal range, $\theta' = 0.78 - 1.0$ rad/2π, to include the solitary vortex and the packet of finer-scale fluctuations, and used data from the last 0.3 s of a 0.5 s single discharge within the spatio-temporal $I_{\rm is}$. Peak times from the cross-correlation were identified, as marked by the red points in Fig. 2(g). Using these peak times as a focal point, the subsequent reference waveform was obtained by averaging the relevant spatio-temporal $I_{\rm is}$ (Fig. 2(b)). This process was repeated: for example, peak times from the cross-correlation between the updated reference waveform ($N = 1$, Fig. 2(b)) and the spatio-temporal $I_{\rm is}$ (Fig. 2(f)) were identified in Fig.2(h). The next iteration for the waveform was then produced, as shown in Fig. 2(c) for $N = 2$. This iterative refinement continued until the $50^{\rm th}$ reference waveform, which had achieved convergence (as demonstrated in

Appendix A). The resulting reference waveform is shown in Fig. 2(e).

The method of reconstructing a cross-sectional structure using the reference waveform is shown below [20]. A visualized explanation is available in Appendix B. The time, t_0, was calculated as the point in time when the correlation occurred between the reference waveform and the spatio-temporal $I_{\rm is}$ of the solitary vortex and the packet of finer-scale fluctuations, where the Galilean transform is applied on the azimuthal probe array data. The delay time for the i-th period, τ, was defined by the equation $\tau = t - t_0(i)$. The relative azimuthal location of the radially movable probe array with respect to the correlation peak of the azimuthal probe array data, θ_i, was also identified. Values from the radially movable probe array were measured simultaneously at various radial positions. For each radius, we reconstructed the azimuthal-temporal structure via the conditional averaging of the values from the radially movable probe array with respect to θ_i and τ. Here, the $I_{\rm is}$ and $V_{\rm f}$ of the radially movable probe array are normalized as $\tilde{I}_{\rm is}/\bar{I}_{\rm is}$ and $eV_{\rm f}/T_{\rm e} \equiv \phi$, where the $\tilde{}$ and $\bar{}$ represent fluctuation components or time averages at each radial position. Thereafter, ϕ denotes the normalized potential . Combining the azimuthal-temporal structure of all the radial positions, an entire region of the cross-sectional structure, $\tilde{I}_{\rm is}/\bar{I}_{\rm is}(\theta, r, \tau)$ or $\phi(\theta, r, \tau)$, was obtained.

The cross-sectional zonal potential was obtained by filtering the $m = 0$ signal from each radial and temporal component. Singular value decomposition (SVD) analysis was used to determine the other components [24, 25]. The waves and the solitary vortex varied with the frequency of the zonal flow ($\sim$0.4 kHz); as a result, the structures were reconstructed by adding the temporally varying structures at 0.4 kHz and its harmonic at 0.8 kHz. The packet of finer-scale fluctuations was then reconstructed by including the structures in the order of the largest singular value of the SVD modes and considering the dimension with the highest correlation coefficient with the azimuthal probe array. The other SVD modes were treated as noise and were therefore not considered in this analysis. The Galilean transformation, which subtracts the linear phase shift of the azimuthal angle along the direction of the wave propagation, is used to make the changes in the reconstructed structures more clearly.

5. Time evolution of two-dimensional spatial structure

Figure 3(a) shows the temporal behaviour of the zonal flow ($m = 0$ fluctuation), $V_{\rm ZF} \equiv \rho \partial\phi/\partial r$, where $\rho = c_{\rm s}/\omega_{\rm Ci} = (eT_{\rm e}/m_{\rm i})^{1/2}/(eB/m_{\rm i}) \approx 1.1$ cm is the Larmor radius, $c_{\rm s}$ is the ion sound velocity, $\omega_{C_{\rm i}}$ is the ion gyro frequency and $m_{\rm i}$ is the mass of argon ($\approx 6.63 \times 10^{-27}$ kg). The two-dimensional azimuthal cross-section image of the potential fluctuation $\tilde{\phi}$ at $\tau = -1$ ms and $\tau = 0$ ms, averaged over a time interval of 0.4 ms, are shown in Figs. 3(b)–(g). Figures 3(b) and (e) show the zonal flow potential, Figs. 3(c) and 1(f) show the waves and the solitary vortex, respectively, and Figs. 3(d) and (g) demonstrate the amplitude envelope of the finer-scale fluctuations. The closed isolines of $\tilde{\phi}$, highlighted in Fig. 3(f) by the dashed ellipse, show the excitation of the solitary vortex because in Fig. 3(c) the $\tilde{\phi}$ at this location is neither closed nor excited.

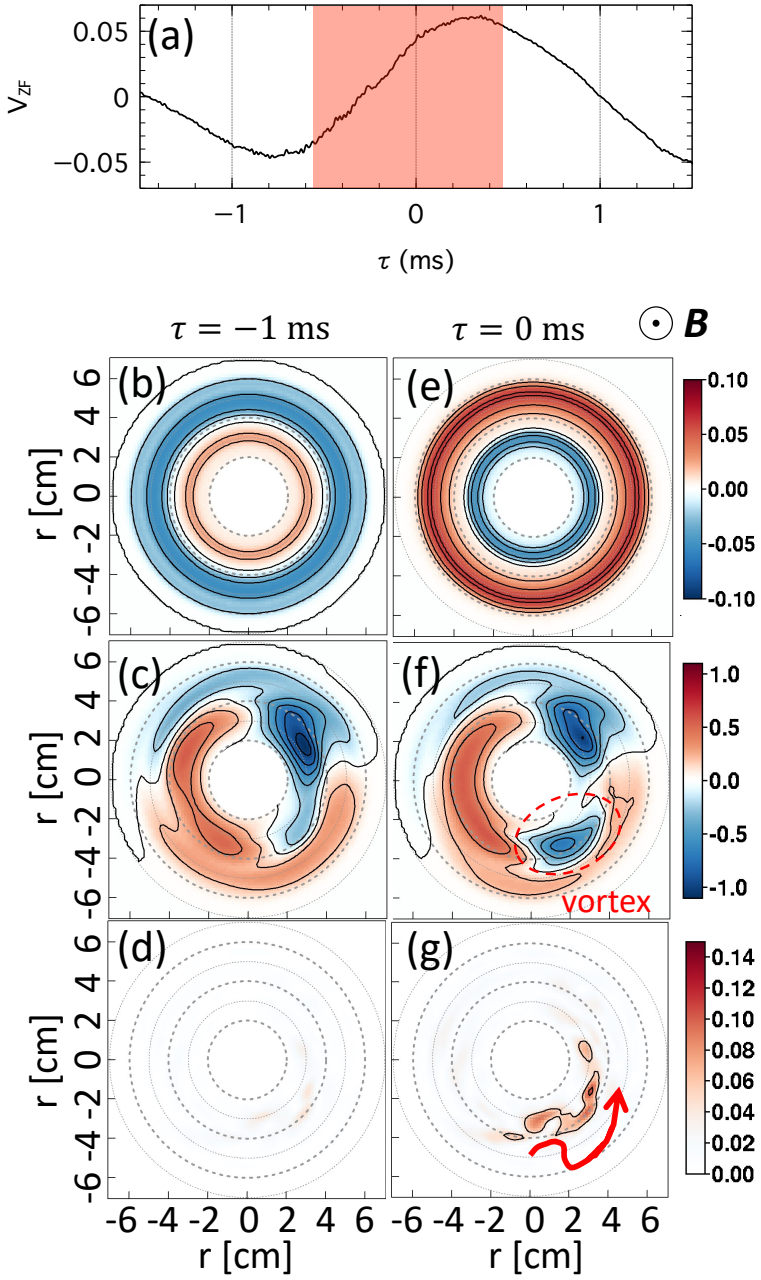

Figure 3. (a) Temporal behavior of the zonal flow (r = 3–4.5 cm). The hatched region shows the time in the excitation of the solitary vortex and the packet of finer-scale fluctuations. (b)–(g) Two-dimensional structure of potential fluctuations for the zonal flow ((b) and (e)), the waves and the solitary vortex ((c) and (f)), and the amplitude envelope of the packet of finer-scale fluctuations ((d) and (g)). (b)–(d) show the structures at τ = -1 ms, and (e)–(g) show the structures at τ = 0 ms. The red arrow in (g) indicates the propagation direction of the packet of finer-scale fluctuations.

The large amplitude in Fig. 3(g) indicates a packet of finer-scale fluctuations being excited, while a small amplitude in Fig. 3(d) shows that it is not excited. The excitation location of the packet of finer-scale fluctuations is equal to that of the solitary vortex, with a ~ 5 cm in the azimuthal direction and a ~ 3 cm in the radial direction. The red arrow next to the fluctuations in Fig. 3(g) indicates the direction of propagation for the finer-scale fluctuation, as shown below.

6. Trapping of the packet of finer-scale fluctuations

The packet of finer-scale fluctuations is trapped by the solitary vortex. Figure 4 shows the time variation in the two-dimensional potential structure of the packet of finer-scale fluctuations. Figures 4(a) to (f) are time-averaged snapshots for $10\,\mu s$ each and show the time at (a) $\tau = -330\,\mu s$, (b) $\tau = -250\,\mu s$, (c) $\tau = -220\,\mu s$, (d) $\tau = -170\,\mu s$, (e) $\tau = -130\,\mu s$, and (f) $\tau = -50\,\mu s$ respectively. The filled contour indicates the potential of the packet of finer-scale fluctuations. The contour lines indicate the potential of the waves and the solitary vortex. The cross mark in each figure indicates the location of the peak of the finer-scale fluctuations at each given moment. The arrow in the figure illustrates the propagation direction of the peak. The movement of the cross marks in time shows that the trajectory of the peaks is particularly radially varying, indicating that they are trapped in the solitary vortex.

The temporal evolution of the potential peak trajectories of the finer-scale fluctuation is explained in Fig. 5. The red-purple cross-lines in Fig. 5 (a) indicate the radial and azimuthal profile axes of the solitary vortex shown in (b) and (d) on the Cartesian coordinate. The Fig. 5(b) or (d) shows the potential profiles of the solitary vortex in the radial or azimuthal direction when $\theta' = 0.84$ rad/(2π) or $r = 3.5$ cm. The Fig. 5(c) or (e) indicates the peak trajectory in the radial or azimuthal direction of the potential of finer-scale fluctuations. Blue or red hatched areas each indicate the trajectory of the same peak, indicating two trappings. The peak meanders from 3 to 4 cm in the radial direction. In the azimuthal direction, it propagates in the electron diamagnetic direction, but pauses $\sim 5 \times 10^{-2}$ ms around $\theta' = 0.85$ rad/(2π) when the peak moves radially. The trapping time of the packet of finer-scale fluctuations in the solitary vortex is $2{\times}10^{-1}$–$3{\times}10^{-1}$ ms.

7. Comparison with theoretical evaluation

The typical time scale of the finer-scale fluctuations circulating around the solitary vortex is close to the bounce time predicted by the trapping theory in a semi-quantitative manner [14, 15]. Using a theoretical evaluation of the bounce frequency for a wave packet trapped in a vortex to the conditions of this study yields $\omega_b = \sqrt{2k_\theta^2 q_r^2 \rho^4 V_G V_*^{-1}(1+k_\theta^2\rho^2)^{-2}} \cdot V_*\rho^{-1} \sim 2 \times 10^4$ rad/s, where k_θ is the azimuthal wavenumber of the finer-scale fluctuations, q_r is the radial wavenumber of the solitary vortex, V_G is the $E \times B$ velocity of the solitary vortex and V_* is the diamagnetic

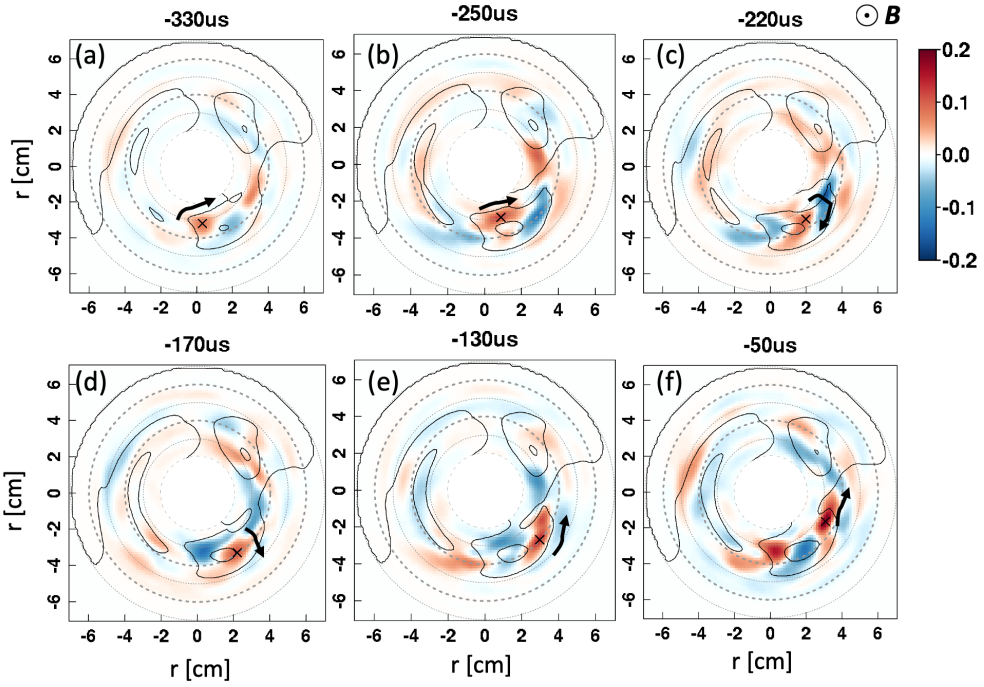

Figure 4. The instantaneous two-dimensional packet of finer-scale fluctuations at (a) $\tau = -330\,\mu s$, (b) $\tau = -250\,\mu s$, (c) $\tau = -220\,\mu s$, (d) $\tau = -170\,\mu s$, (e) $\tau = -130\,\mu s$, and (f) $\tau = -50\,\mu s$. The filled contour indicates the potential (ϕ) of the packet of finer-scale fluctuations and the contour lines indicates the potential of the waves and the solitary vortex. The cross-mark represents the instantaneous potential peak of the finer-scale fluctuations. The arrows indicate the guides of the propagating fluctuation peak.

drift velocity; the parameters are $k_\theta \rho \sim 4 \times 10^{-1}$, $q_r \rho \sim 4 \times 10^{-1}$, $V_G V_*^{-1} \sim 1$ and $V_* \sim 1 \times 10^3\,\mathrm{m/s}$. The evaluated trapping time is $2\pi/\omega_b \sim 3{\times}10^{-1}\,\mathrm{ms}$, which is close to the experimental value ($2{\times}10^{-1}$–$3{\times}10^{-1}\,\mathrm{ms}$). It is noted that the aforementioned theory is based on one-dimensional analysis; the inhomogeneity of the solitary vortex in the azimuthal direction is not taken into account.

8. Summary

In conclusion, turbulence excitation experiments were conducted in a linear magnetized plasma. Frequency filters and singular value decomposition were used to differentiate among zonal flows, drift wave-type modes, and solitary vortex and packet of finer-scale fluctuations. A modified template method was used to reconstruct time-varying two-dimensional cross-sectional structures. Peak tracking of the packet of finer-scale fluctuations revealed that fluctuations are observed to be trapped by the solitary vortex, particularly in the radial direction. The trapping times observed ranging from 0.2 to 0.3 ms, which is consistent with the one-dimensional theoretical evaluation.

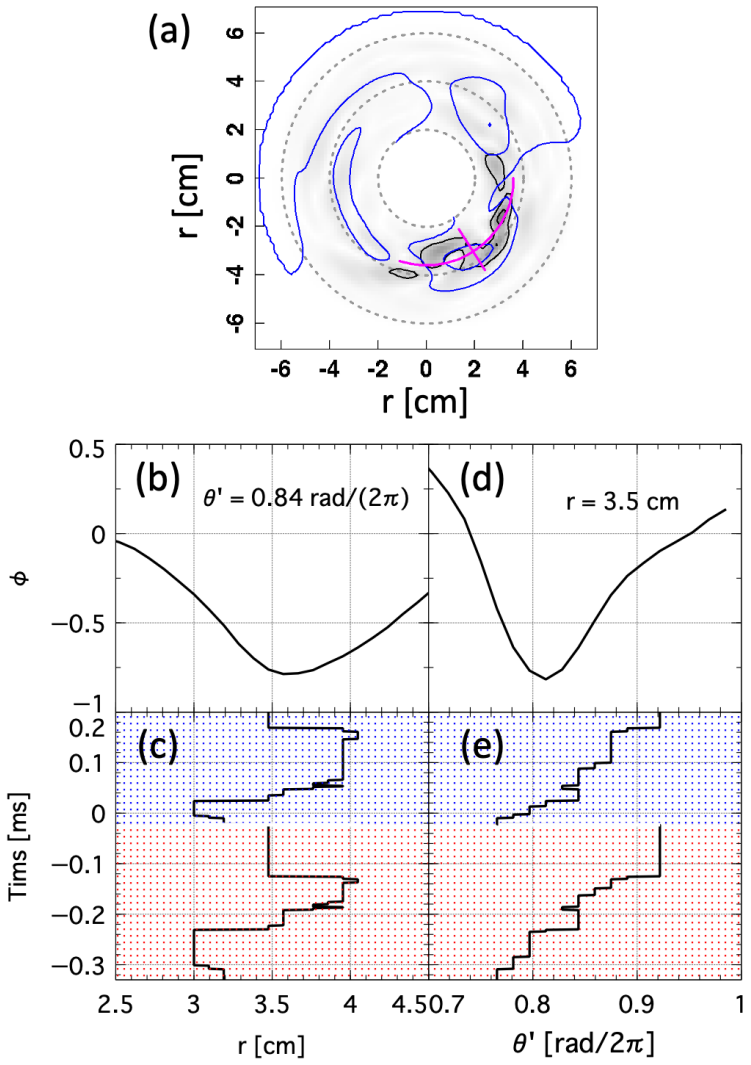

Figure 5. Peak propagation of finer-scale fluctuations in the cylindrical coordinate system. (a) The radial and azimuthal axes of the solitary vortex are shown in (b) and (d) on the Cartesian coordinates (red-purple cross-lines). The contour lines show the potential fluctuation of the waves and the solitary vortex. The filled contour represents the amplitude of the finer-scale fluctuations. (b) The radial profile of the solitary vortex at a azimuthal condition ($\theta' = 0.84$ rad/(2π)). (c) Peak propagation in the radial direction of the packet of finer-scale fluctuations. The ranges in which the same peaks propagate are indicated by the red or blue hatching region, respectively. (d) Azimuthal profile of the solitary vortex at $r = 3.5$ cm condition. (e) Peak propagation in the azimuthal direction of the finer-scale fluctuations.

Acknowledgments

This work has been supported by the grant-in-aid for Scientific Research of JSPS KAKENHI (Grant Numbers JP17K14897, JP17H06089, JP15H02335, JP15H02155, JP21K03513 and JP21K03508), by the Collaborative Research Programme of Research Institute for Applied Mechanics, Kyushu University, by the Shimadzu Science Foundation, by the NIFS Collaboration Research program (NIFS17KOCH002), by the Agence Nationale de la Recherche for the project GRANUL (ANR-19-CE30-0005) and by the Asada Science Foundation.

Appendix A. Convergence of two-dimensional reference waveform

The convergence of the reference waveform was validated using the correlation coefficient as it was iteratively refined. Figure A1 displays this correlation coefficient shown against the number of iterations. Specifically, the iteration number refers to the correlation between successive reference waveforms. For instance, the 2^{nd} iteration point on the graph represents the correlation coefficient between the 1^{st} (Fig. 2(b)) and 2^{nd} (Fig. 2(c)) reference waveforms. The correlation coefficient reached 1 at the 8^{th} iteration or more. This indicates that the reference waveform is in perfect agreement with the previous reference waveform at the 8^{th} iteration or more.

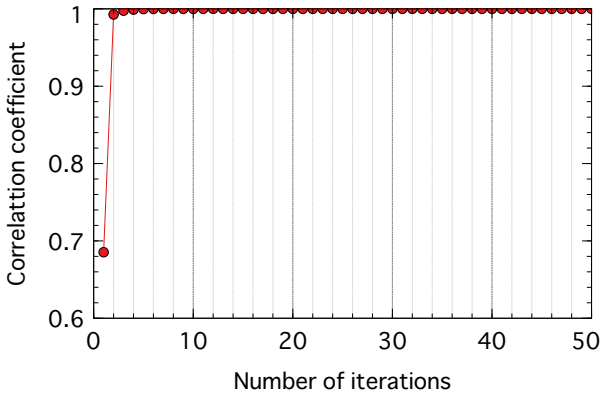

Figure A1. Correlation coefficient of the reference waveform versus number of iterations.

Appendix B. Two-dimensional reconstruction with conditional averaging [20]

Figure B1 shows the method used for timing detection and for determining the conditions during conditional averaging. Figure B1(a) displays the spatio-temporal I_{is} with the Galilean transform applied to the azimuthal probe array data. This covers a partial azimuthal range of $\theta' = 0.78 - 1.0$ rad$/2\pi$, which includes the solitary vortex and the

packet of finer-scale fluctuations. In Figure B1(b), the cross-correlation function between $I_{\rm is}$ and the reference waveform (as seen in Fig. 2(e)) is depicted, with the correlation peaks highlighted by red points. The reference waveform is centered at $\tau = 0$, a point when the density of the solitary vortex and the packet of finer-scale fluctuations reaches its peak within the azimuthal probe array data, thus the correlation peak is observed at this timing. As shown in Section 3, the waves, which include the drift wave-type mode and its harmonics, propagate in the electron diamagnetic direction. The timing of these correlation peaks and this propagation (shown in Fig. B1(c)) can be matched based on the azimuthal angle. On the other hand, the position of the radially movable probe is fixed at a specific azimuthal position. Therefore, the timing and relative azimuthal location (to the waves) of the radially movable probe can be determined similarly. Based on correlation peak timings, values (ϕ and $\tilde{I}_{\rm is}/\bar{I}_{\rm is}$) were obtained from the radially movable probe located at a particular radial position (as shown in Fig.B1(d), only ϕ is described as an example). For example, at the timing of the correlation peaks in the figure, $t_0(i)$, relative azimuthal location of radially movable probe, θ_i, was ascertained. In turn, $\phi(t_0(i), r)$ was also obtained by the radially movable probe. Consequently, ϕ is provided under conditions based on r and θ_i, relative to the waves.

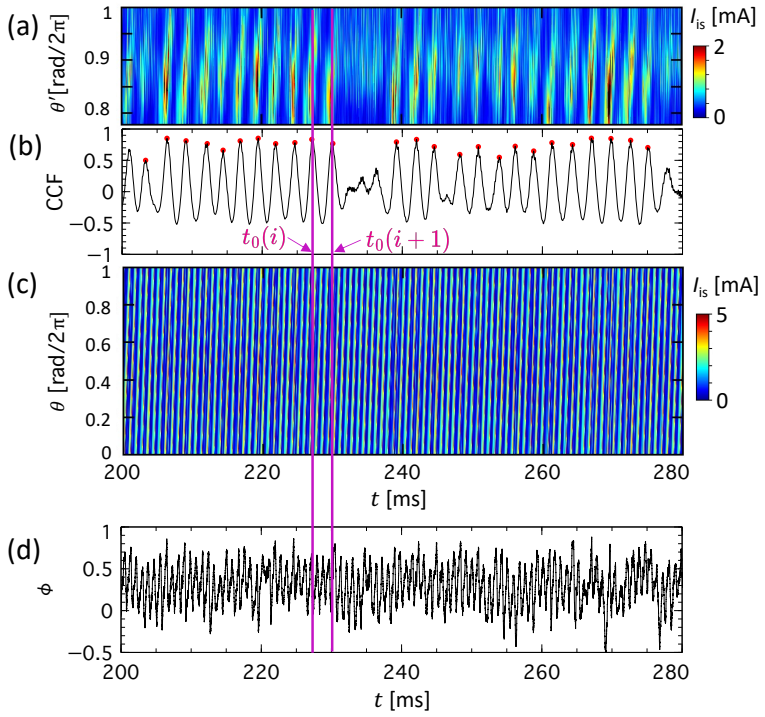

Figure B1. (a) A spatio-temporal $I_{\rm is}$ of a partial azimuthal range, $\theta' = 0.78 - 1.0$ rad/2π, from the azimuthal probe array. (b) Cross-correlation function (CCF) between (a) and the reference waveform (Fig. 2(e)), where the $t_0(i)$ and the $t_0(i+1)$ are the time at the i-th correlation peaks. (c) Corresponding spatio-temporal $I_{\rm is}$ from the azimuthal probe array before the Galilean transformation. (d) A potential of movable probe installed at a radial and a azimuthal position measured simultaneously.

The method of conditional averaging for two-dimensional reconstruction is illustrated in Fig. B2, taking the timings of $t_0(i)$ and $t_0(i+1)$ in Fig. B1 as examples. Figure B2(a) and (b) show the relative two-dimensional positions, θ_i and θ_{i+1}, of the radially movable probe at the times $t_0(i)$ and $t_0(i+1)$, respectively, in relation to the azimuthal angles of the waves. Setting these timings as $\tau = 0$, transformations are applied such that $\tau = t - t_0(i)$ and $\tau = t - t_0(i+1)$. This approach facilitates the determination of ϕ in two-dimensional space at $\tau = 0$ for the radial position (r) and relative azimuthal angles θ_i or θ_{i+1} as depicted in Fig. B2(c). Given that the waves propagation angle around $\tau = 0$ while the movable probe remains stationary, the relationship between the propagating structures at time $\tau = \xi$ can be visualized, as in Fig. B2(d). Figure B2(e) demonstrates the azimuthal relationship of τ dependence between the propagating structure and the movable probe. This relationship stems from the propagation of the waves during the Galilean transformation applied to the azimuthal probe array data. The orange lines in Fig. B2(e) denote the peaks recognized before and after the timing $t_0(i)$ as shown in Fig. B2(a), while the purple lines represent the peaks observed before and after the timing $t_0(i+1)$ as illustrated in Fig. B2(b). The positions of these orange and purple lines align with the potential ϕ values derived from the movable probe, as shown in Fig. B2(f) and (g). Since these values are tied to specific radii (r), the temporal sequence of ϕ in a two-dimensional setting was reconstructed by pinpointing the azimuthal angles corresponding to the various radial positions (0.5 cm intervals) and correlation peaks. In total, 2596 correlation peaks were identified, which, when conditionally averaged, spanned the entire region, enabling the reconstruction of the two-dimensional structure.

Data availability statement

Data are available upon reasonable request.

Competing financial interests

The authors declare no competing financial interests.

References

[1] P. H. Diamond, S.-I. Itoh, K. Itoh, and T. S. Hahm 2005 *Plasma Phys. Control. Fusion* **47** 35–161
[2] K. Itoh, K. Hallatschek, S.-I. Itoh, P.H. Diamond, and S. Toda 2005 *Phys. Plasmas* **12**(6) 062303
[3] A. Fujisawa 2009 *Nucl. Fusion* **49** 013001
[4] M. Nakata, T.H. Watanabe, and H. Sugama 2012 *Phys. Plasmas* **19**(2) 022303
[5] Z. Yan, G.R. McKee, R. Fonck, P. Gohil, R.J. Groebner, and T.H. Osborne 2014 *Physi. Rev. Lett.* **112**(12) 125002
[6] G.D. Conway, A.I. Smolyakov, and T. Ido 2021 *Nucl. Fusion* **62**(1) 013001
[7] G.R. Tynan, A. Fujisawa, and G. McKee 2009 *Plasma Phys. Control. Fusion* **51** 113001
[8] P. Manz, M. Xu, S.C. Thakur, and G.R. Tynan 2011 *Plasma Physics and Controlled Fusion* **53**(9) 095001

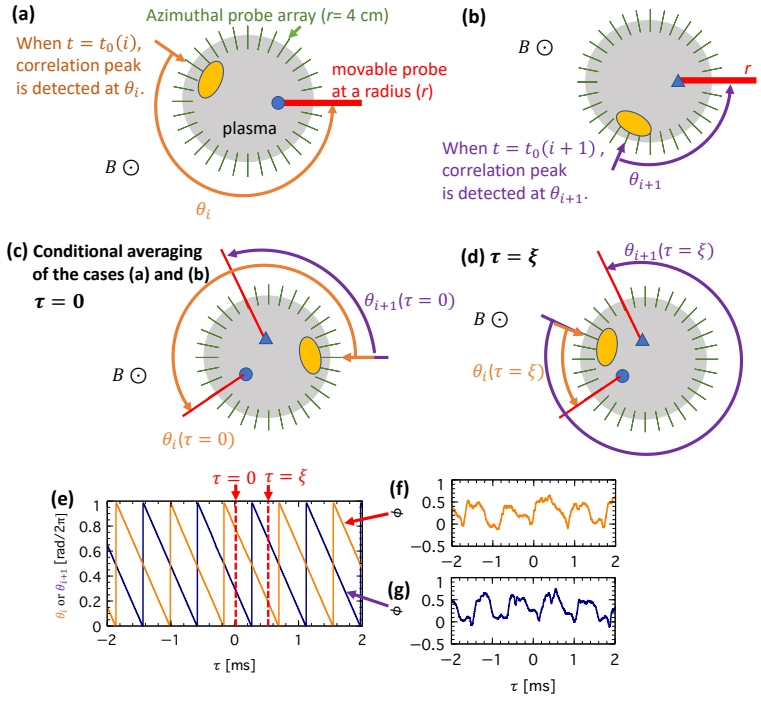

Figure B2. (a) and (b) The relative azimuthal positions of the movable probe in two-dimensional space at time points $t_0(i)$ and $t_0(i+1)$, respectively. (c) The two-dimensional position of the movable probe at $\tau = 0$, relative to the propagating waves depicted in (a) and (b). (d) Two-dimensional relationships at timing $\tau = \xi$. (e) The τ-dependence of azimuthal positional relationships. The orange and purple lines represent the positions θ_i and θ_{i+1}, respectively. (f) and (g) The respective τ-dependencies of ϕ as measured by the movable probe.

[9] R. Hong, J.C. Li, S.C. Thakur, R Hajjar, P.H. Diamond, and G.R. Tynan 2018 *Physi. Rev. Lett.* **120**(20) 205001

[10] T.A. Carter and J.E. Maggs 2009 *Phys. Plasmas* **16**(1)

[11] C. Brandt, S.C. Thakur, A.D. Light, J. Negrete Jr, and G.R. Tynan 2014 *Physi. Rev. Lett.* **113**(26) 265001

[12] D.A. Schaffner, T.A. Carter, G.D. Rossi, D.S. Guice, J.E. Maggs, S. Vincena, and B. Friedman 2012 *Physi. Rev. Lett.* **109**(13) 135002

[13] J. T. Ma, W. W. Xiao, C. Y. Wang, W. J. Zhong, and Niaz Wali 07 2023 *Phys. Plasmas* **30**(7) 072301

[14] P. Kaw, R. Singh, and P.H. Diamond 2001 *Plasma Phys. Controll. Fusion* **44**(1) 51

[15] M. Sasaki, K. Itoh, K. Hallatschek, N. Kasuya, M. Lesur, Y. Kosuga, and S.-I. Itoh 2017 *Sci. Rep.* **7**(1) 1–7

[16] M Sasaki, T Kobayashi, K Itoh, N Kasuya, Y Kosuga, A Fujisawa, and S-I Itoh 2018 *Phys. Plasmas* **25**(1) 012316

[17] X. Garbet, O. Panico, R. Varennes, C. Gillot, G. Dif-Pradalier, Y. Sarazin, V. Grandgirard, P. Ghendrih, and L. Vermare 2021 *Phys. Plasmas* **28**(4) 042302

[18] M. Sasaki, K. Itoh, B.F. McMillan, T. Kobayashi, H. Arakawa, and J. Chowdhury 2021 *Phys. Plasmas* **28**(11) 112304

[19] M. Sasaki, H. Arakawa, T. Kobayashi, F. Kin, Y. Kawachi, T. Yamada, and K. Itoh 2021 *Phys. Plasmas* **28**(10) 102304

[20] H. Arakawa, M. Sasaki, S. Inagaki, Y. Kosuga, T. Kobayashi, N. Kasuya, T. Yamada,

Y. Nagashima, F. Kin, A. Fujisawa, K. Itoh, and S.-I. Itoh 2019 *Phys. Plasmas* **26**(5) 052305

[21] H. Arakawa, M. Sasaki, S. Inagaki, M. Lesur, Y. Kosuga, T. Kobayashi, F. Kin, T. Yamada, Y. Nagashima, A. Fujisawa, and K. Itoh 2022 *Plasma Fusion Res.* **17** 1301106–1301106

[22] Y. Nagashima, S.-I. Itoh, S. Shinohara, M. Fukao, A. Fujisawa, K. Terasaka, Y. Kawai, G.R. Tynan, P.H. Diamond, M. Yagi, *et al* 2009 *Phys. Plasmas* **16** 020706

[23] S. Inagaki, Y. Miwa, T. Kobayashi, T Yamada, Y. Nagashima, T. Mitsuzono, H. Fujino, M. Sasaki, N. Kasuya, M. Lesur, Y. Kosuga, A Fujisawa, S.-I. Itoh, and K. Itoh 2014 *Plasma Fusion Res.* **9** 1201016

[24] E.R. Henry and J. Hofrichter. [8] Singular Value Decomposition: Application to analysis of experimental data. In *Numerical Computer Methods*, volume 210 of *Methods in Enzymology*, pages 129–192. Academic Press, 1992.

[25] M Sasaki, T Kobayashi, RO Dendy, Y Kawachi, H Arakawa, and S Inagaki 2021 *Plasma Phys. Controll. Fusion* **63**(2) 025004